AGU PUBLICATIONS

JGR

Journal of Geophysical Research: Oceans

RESEARCH ARTICLE

10.1002/2013JC009733

Special Section:
Western Pacific Ocean Circulation and Climate

Key Points:
- SST and SSS show (semi) annual oscillations in the (Bismarck) Solomon Sea
- These oscillations result mainly from horizontal advection in both seas
- Coastal upwelling and Sepik River discharge also important in the Bismarck Sea

Correspondence to:
T. Delcroix,
Thierry.Delcroix@ird.fr

Citation:
Delcroix, T., M.-H. Radenac, S. Cravatte, G. Alory, L. Gourdeau, F. Léger, A. Singh, and D. Varillon (2014), Sea surface temperature and salinity seasonal changes in the western Solomon and Bismarck Seas, *J. Geophys. Res. Oceans*, *119*, doi:10.1002/2013JC009733.

Received 13 DEC 2013
Accepted 20 MAR 2014
Accepted article online 24 MAR 2014

Sea surface temperature and salinity seasonal changes in the western Solomon and Bismarck Seas

Thierry Delcroix[1], Marie-Hélène Radenac[1], Sophie Cravatte[2], Gaël Alory[1], Lionel Gourdeau[1], Fabien Léger[1], Awnesh Singh[3], and David Varillon[4]

[1]LEGOS, UMR 5566, CNES, CNRS, IRD, Université de Toulouse, Toulouse, France, [2]LEGOS, Centre IRD de Nouméa, Nouméa, New Caledonia, [3]PACE-SD, University of the South Pacific, Suva, Fiji, [4]US IMAGO, Centre IRD de Nouméa, Nouméa, New Caledonia

Abstract We analyze mean and seasonal change of Sea Surface Temperature (SST) and Salinity (SSS) in the Solomon and Bismarck Seas, using 1977–2009 in situ data collected from Voluntary Observing Ships. Covariability of these two variables with surface wind, altimeter-derived and model-derived horizontal currents, precipitation, and Sepik River discharge are examined. SST and SSS show large annual oscillations in the Solomon Sea, with the coldest and saltiest waters occurring in July/August mainly due to horizontal advection. In contrast, they show large semiannual oscillations in the Bismarck Sea. There, the coldest and saltiest waters happen in January/February, when the northwest monsoon winds drive coastal upwelling, and in July/August, when the New Guinea Coastal Current advects cold and high-salinity waters from the Solomon Sea through Vitiaz Strait. The low SSS values observed in April/May, stuck between the January/February and July/August SSS maxima, are further enhanced by the Sepik River discharge annual maximum. A high-resolution model strengthens the conclusions we derive from observations. The impacts of ENSO on SST and SSS are also discussed with, for instance, saltier-than-average and fresher-than-average waters during the 2002–2003 El Niño and 2007–2008 La Niña, respectively.

1. Introduction

Papua New Guinea (PNG) is the largest Pacific Island nation. Its landmass lies in the western tropical Pacific within about 2°S–12°S and 141°E–156°E. It consists of the eastern half of the island of New Guinea together with numerous easterly located islands such as Manus, New Britain, New Ireland, and Bougainville. PNG is delimited by the Coral Sea to the Southeast and by the Solomon and Bismarck Seas to the Northeast (see Figure 1a). These seas are located in the western part of the so-called warm pool region and, as such, have some of the warmest waters in the global ocean. There, the annual mean Sea Surface Temperature (SST) ranges within 28°C–29.5°C (Figure 2a), which is equal or over the usual threshold for deep atmospheric convection [*Waliser and Graham*, 1993]. As a consequence, small SST changes in these warm waters may have strong global climatic impact, and may further be of importance for the onset of El Niño Southern Oscillation (ENSO) events [*Palmer and Mansfield*, 1984; *World Climate Research Program*, 1990; *Hasegawa et al.*, 2009; *Ramesh and Murtugudde*, 2012]. This region is further characterized by the world oceans' greatest occurrence rate of "hot events," defined as SST warmer than 30°C [*Qin et al.*, 2007].

In line with warm SST and associated deep atmospheric convection, the regional Precipitation (P) is rather high, ranging from 0.1 to 0.6 m/month (Figure 3), with notable spatial variability due to orographic effects [*Xie and Arkin*, 1998; *Smith et al.*, 2013]. The in-land PNG rainfall flows to the sea through several rivers, such as the Sepik River into the Bismarck Sea and the Markham River in Huon Gulf into the Solomon Sea (see Figure 1a). Because of high rainfall, luxuriant vegetation, high mountains (almost half of the PNG area is over 1000 m above sea level, Figure 1a, with Mount Wilhem reaching 4509 m in height), and tectonically active areas, these rivers release a huge amount of terrestrial material to the ocean. The derived global sediment discharge entering the ocean through PNG Rivers has been estimated as 1.8×10^9 t/yr, i.e., comparable to that of the Amazon River [cf. *Milliman and Farnsworth*, 2011]. When entering the ocean, directly or indirectly via PNG rivers, rainfall water and sediment discharge have been shown—or are thought—to affect Sea Surface Salinity (SSS), water stratification, vertical mixing, light penetration, supply of nutrients, and phytoplankton distribution within the region [*Cresswell*, 2000; *Kineke et al.*, 2000; *Higgins et al.*, 2006; *Burns et al.*, 2008]. Farther away, the iron-rich sediments of the Sepik and Ramu rivers may be transported by the mean oceanic

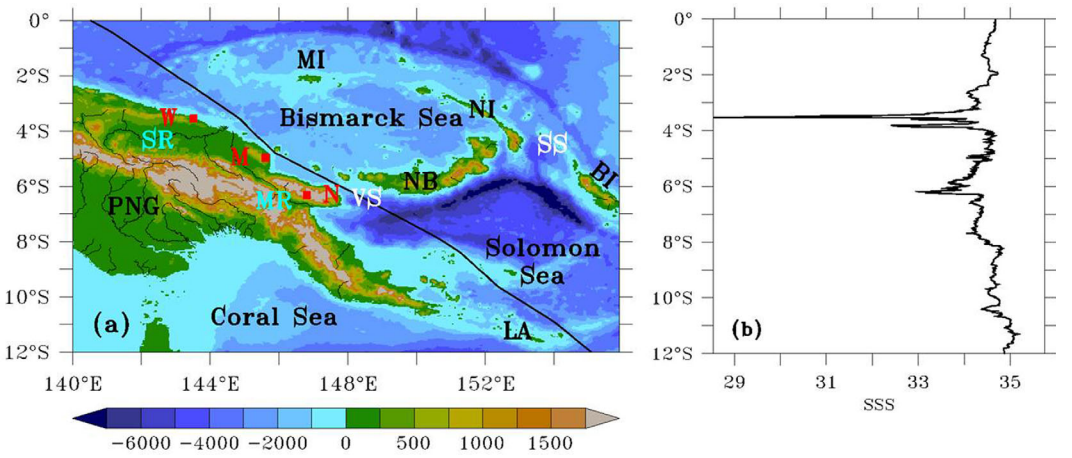

Figure 1. (a) Bathymetry below sea level and topography above sea level (in m) of the New Guinea region. Acronyms denote: *PNG* Papua New Guinea, *NB* New Britain, *NI* New Ireland, *BI* Bougainville Island, *MI* Manus Island, *LA* Louisiades Archipelago, *SS* Solomon Strait, *VS* Vitiaz Strait, *SR* Sepik River, *MR* Markham River, and the cities of *W* Wewak, *M* Madang, and *N* Nadzab. (b) Sea Surface Salinity measured from a TSG instrument along the route shown as a thin black line in Figure 1a of the M/V Tropical Islander during December 2009.

circulation to the Equatorial Undercurrent (EUC), and then partly control new primary production in the eastern and central equatorial Pacific [*Mackey et al*., 2002; *Ryan et al*., 2006; *Grenier et al*., 2011; *Slemons et al*., 2013].

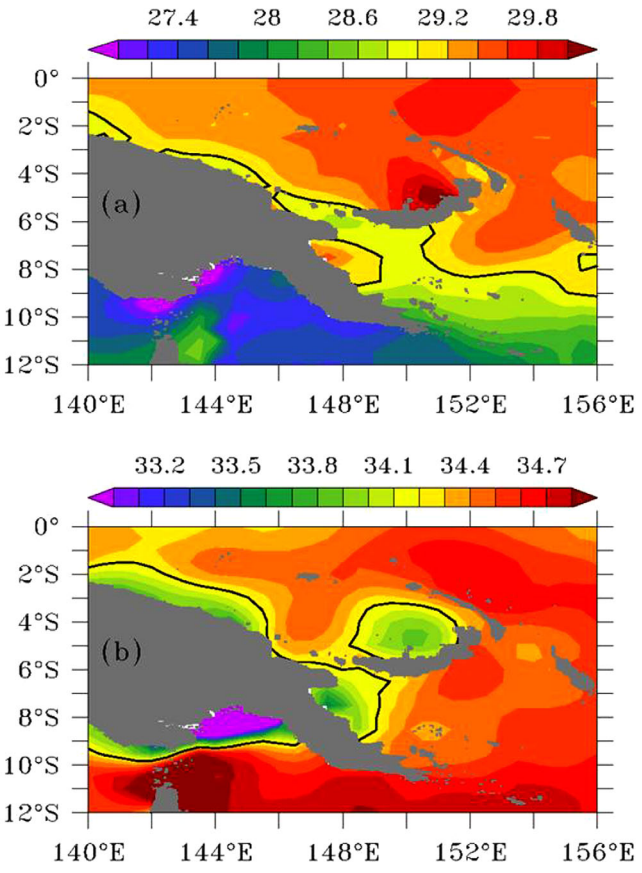

Figure 2. Mean (a) Sea Surface Temperature and (b) Sea Surface Salinity in the PNG region, as obtained from the CARS data sets (see section 2). The heavy black lines denote the 29°C isotherm in Figure 2a and the 34.3 isohaline in Figure 2b. Unit for SST is °C.

One key element of the regional climate variability is the seasonal latitudinal migration of the Inter-Tropical and South Pacific Convergence Zones (ITCZ and SPCZ, respectively). When the related wind convergence is north of PNG, roughly from May to October, south-easterly (trade) winds blow over the Coral, Solomon, and Bismarck Seas, bringing maximum seasonal rainfall east of New Britain in the Solomon Sea (see Figure 3b, for the month of August). When the wind convergence is above or south of PNG, from about November to April, north-westerly monsoon winds predominate, bringing maximum seasonal rainfall over PNG and west of New Britain in the Bismarck Sea (see Figure 3a, for the month of February). The regional climate also varies from year to year due to ENSO events, as discussed in the last section. Other basic information on the regional climate variability can be obtained from the Pacific Climate Change Science Program web site (PCCSP; see the Acknowledgments section).

In the Bismarck and Solomon Seas, the ocean surface circulation is now

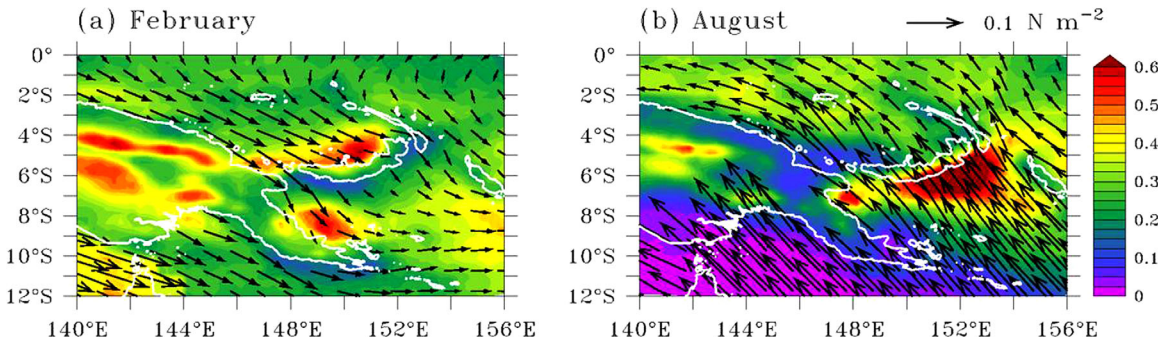

Figure 3. Mean precipitation (color codes; m/month) and wind stress (arrows; N/m^2) in the PNG region for the months of (a) February and (b) August, as obtained from the TRMM and QuikSCAT data sets, respectively (see section 2). The wind stress arrow is scaled in the right plot.

relatively well known. It has been described in the literature thanks to early skillful interpretation of sporadic hydrographic data and, more recently, from analyses of data sets derived from Ship-mounted Acoustic Doppler Current Profilers (SADCP), surface drifters, sea level obtained from tide gauges and altimetry, moorings, and forced models [*Wyrtki*, 1961; *Hisard et al*., 1969; *Lindstrom et al*., 1987; *Ridgway et al*., 1993; *Butt and Lindstrom*, 1994; *Cresswell*, 2000; *Mackey et al*., 2002; *Ueki et al*., 2003; *Melet et al*., 2010a, 2010b, 2013; *Cravatte et al*., 2011; *Hristova and Kessler*, 2012]. All these data and models overall agree on the following circulation pattern.

The mean surface flow enters the Solomon Sea from both its northern and southern parts. From the north, the flow is southward through Solomon Strait; one part flows along the New Britain coast and exits northward through Vitiaz Strait; the other part flows southward into the Solomon Sea, exiting through its southern limit. From the South, the westward-flowing North Vanuatu Jet (NVJ), part of the South Equatorial Current (SEC), joins with the northward-flowing New Guinea Coastal Current (NGCC) to enter east of the Louisiades Archipelago, and also exits through Vitiaz Strait, continuing along the PNG coast. Further offshore, the mean surface circulation appears to be weak and actually not well defined. A useful picture of the mean surface circulation obtained from surface drifters can be found in *Hristova and Kessler* [2012, Figure 2a]. This circulation is varying at seasonal time scales. In austral winter, during the trade wind season, the surface flow is mostly northwestward inside the Solomon Sea, the NGCC is maximum and a strong flow enters the Bismarck Sea through Vitiaz Strait. In austral summer, during the northwesterly monsoon season, the surface currents are mostly southeastward inside the Solomon Sea, and the NGCC flows southeastward west of Vitiaz Strait in the Bismarck Sea. The northwestward flow in Vitiaz Strait is much weaker, and may exceptionally reverse. Changes in the circulation do occur at ENSO time scales as discussed in the last section.

As a complement to the previously cited papers and results, and in line with the international CLIVAR-endorsed SPICE (Southwest Pacific Ocean Circulation and Climate Experiment) [*Ganachaud et al*., 2008] program, the aims of the present study are to describe the regional mean and seasonal variability of SST and, for the first time, Sea Surface Salinity (SSS) structures, and to suggest mechanisms for such variability. This is done relying on a unique set of in situ observations and model outputs. The in situ observations are chiefly obtained from Voluntary Observing Ship (VOS) programs collecting SST and SSS data for more than three decades along commercial shipping lines crossing the western Solomon and Bismarck Seas via the Vitiaz Strait (Figures 1a and 1b). The model outputs are obtained from a global high-resolution (1/12°) primitive equations model that can handle the complex regional bathymetry and resolve the above mentioned narrow straits [see *Gourdeau et al*., 2014]. The rest of the manuscript is organized as follows: section 2 describes the VOS data, additional data used for the interpretation, and data processing; section 3 describes the mean and standard deviation in SSS and SST; section 4 analyses the SSS and SST seasonal variability both from observational and model results; and a discussion and conclusions follow in section 5.

2. Data and Methods

VOS SSS and SST data. The original SSS and SST data analyzed here originate from: (a) surface samples collected from 1969 to 1992 via a tropical Pacific ORSTOM Voluntary Observing Ship (VOS) program operated

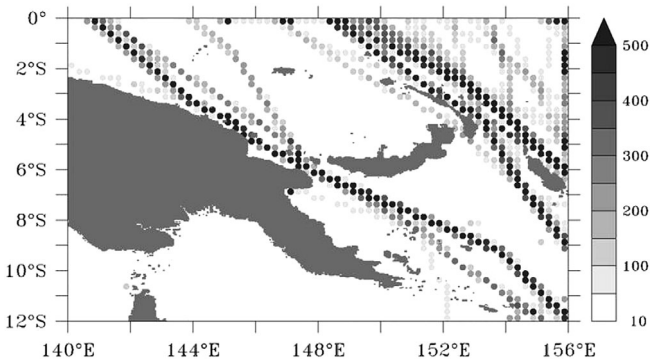

Figure 4. Number of SSS observations per 0.25° latitude by 0.25° longitude square, as collected during 1977–2009. A similar figure would hold for SST.

from New Caledonia, (b) thermosalinograph (TSG) underway measurements collected from 1991 to 2002 via a replacing VOS program operated by IRD (previously named ORSTOM), (c) TSG measurements collected since 2003 via a global VOS program operated by the French SSS Observation Service, and (d) to a lesser extent (2%), near-surface (0–10 m) hydrocasts, salinity-temperature-depth (STD), conductivity-temperature-depth (CTD), and ARGO data. Details about the VOS programs, bucket samples, TSG installation and maintenance, data sampling, bias correction, detection and rejection of outliers, and quality control procedures can be found in the literature, including papers by *Donguy and Hénin* [1976], *Hénin and Grelet* [1996], *Prunier-Mignot et al*. [1999], *Delcroix et al*. [2005], and G. Alory et al. (manuscript in preparation, 2014). Note that salinity computations are based on the Practical Salinity Scale PSS-78, and reported with no units. Once validated, it is worth reminding here that the accuracy of the surface samples and TSG measurements is expected to be of the order of 0.1 and 0.02 for SSS, and 0.1°C and 0.05°C for SST, respectively.

The above-noted VOS programs have been providing SSS and SST measurements along regular ship routes crossing the tropical Pacific Ocean for more than three decades. Some of these routes, to be analyzed here, extend from New Caledonia to Southeast Asia and cross the western part of the Solomon and Bismarck Seas, passing through Vitiaz Strait (see Figure 4). (Note that measurements located in the upper right corner of Figure 4, parallel to Solomon Islands and New Britain will be analyzed in a following study). As an example, the M/V Tropical Islander shipping route of December 2009 (during an El Niño event) is shown in Figure 1, together with the collected TSG-derived SSS data. Interestingly, the along-track data show a -4 to -5 SSS drop at the latitude of the Sepik River and a smaller -1 SSS drop at the latitude of Vitiaz Strait.

Considering the spatial distribution of all VOS data collected in the western part of the Solomon and Bismarck Seas (Figure 4) [see also *Delcroix and McPhaden*, 2002, Figure 1a], we grouped all data into a mean track of about 50 km width. The latitude-time distribution of the SSS data along this mean track (about 95,000 records) is shown in Figure 5 from 1977 to 2009 (a similar figure would hold for SST). This demonstrates the irregular and low spatial resolution of the bucket samples before the 1990s, the high (2–3 km) along-track resolution of the TSG measurements thereafter, as well as the occurrence of three well-sampled periods (1983–1985, 1992–1994, and 1999–2009, which include 92% of the total records), denoting more intense commercial traffics along this shipping route. This irregularly distributed data, both in space and time, were gridded onto a 1 month $\times$ 0.25° latitude grid using Laplacian interpolation as in *Delcroix and Hénin* [1991]. Data gaps exceeding twice the grid element sizes, i.e., 2 months and 0.5° latitude, were not filled in. Standard deviation values and monthly climatology in SSS and SST were then computed both over the maximum length of the time series (i.e., 1977–2009), and over the three well-sampled periods only (i.e., 1983–1985 + 1992–1994 + 1999–2009). The results were identical whatever the chosen time period, and values computed over 1977–2009 are presented here.

Altimetry-derived surface geostrophic current anomaly. Sea level anomalies relative to the 1993–1999 mean state, as distributed by the CTOH at LEGOS [see *Birol et al*., 2010; *Roblou et al*., 2011], were used to compute surface geostrophic current anomalies along seven satellite ground tracks roughly perpendicular to the north coast of PNG. The distance between successive tracks is of the order of 315 km at the equator. The current anomaly was calculated as a weighted sum of the geostrophic velocity anomaly calculated in the f-plane and β-planes away and near the equator, respectively, following the method of *Picaut and Tournier* [1991] and revised by *Lagerloef et al*. [1999]. We then constructed a monthly climatology by averaging cross-track geostrophic current anomaly of the original 10 day period time series from January 1994 to December 2010. Details can be found in M.-H. Radenac et al. (manuscript in preparation, 2014).

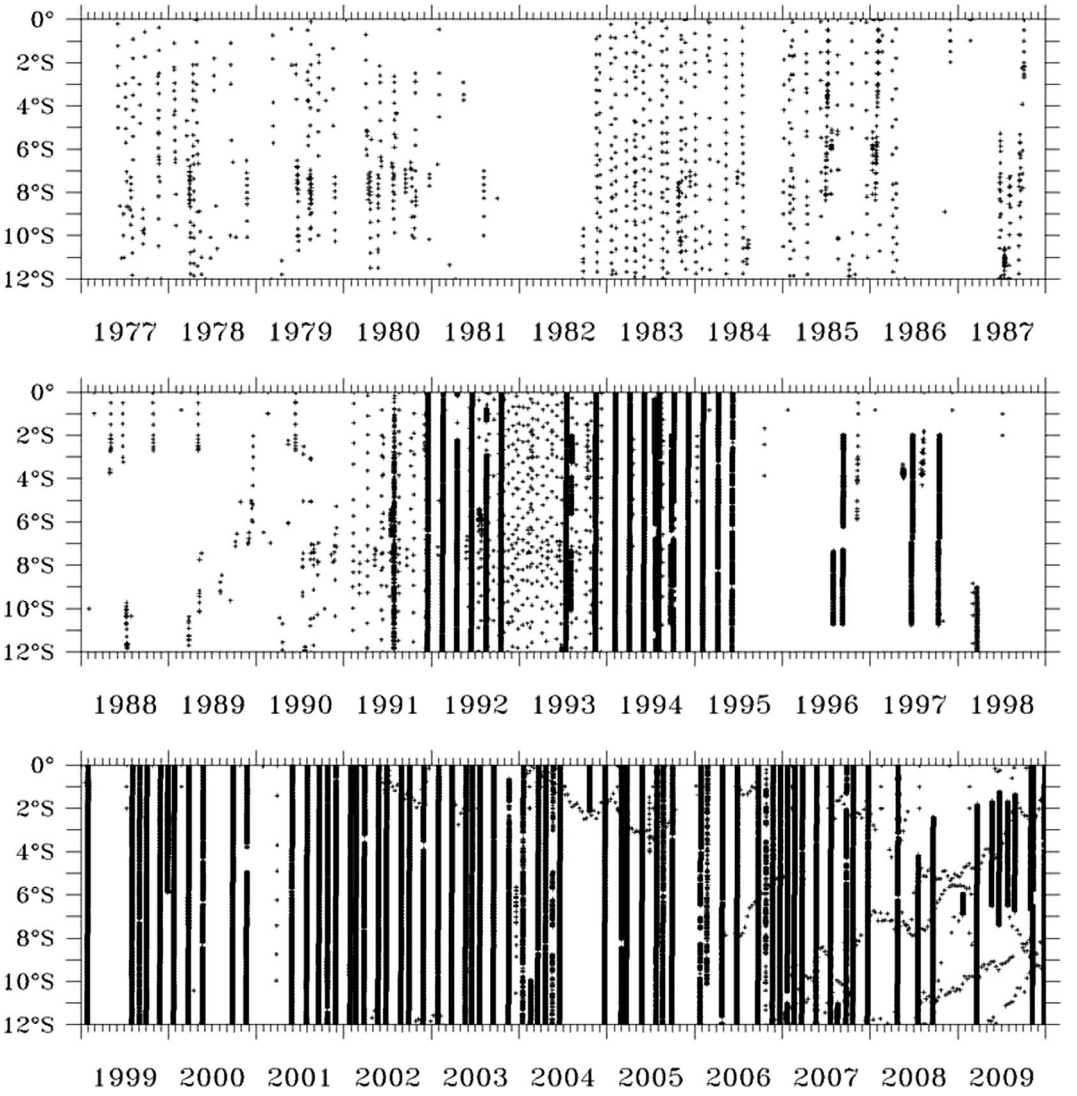

Figure 5. Latitude-time diagram of SSS data collected along the mean ship track crossing the Solomon and Bismarck Seas via Vitiaz Strait, as exemplified in Figure 1a. A similar figure would hold for SST.

Precipitation and river flow. At the time of writing, there are about one dozen of available gridded rainfall products with different resolutions and time periods [see *Smith et al*., 2013]. Here we use the monthly 2.5° longitude by 2.5° latitude 1979–2012 CMAP (Climate Prediction Center Merged Analysis of Precipitation) product [*Xie and Arkin*, 1998] and the 1979–2008 GPCP (Global Precipitation Climatology Project) product [*Adler et al*., 2000] available on the same grid mesh. These two products comprise both satellite-based estimates over the ocean and rain gauge measurements over land. We also use the monthly TRMM (Tropical Rainfall Measuring Mission) satellite-only-based product, which is available on a $^1/_4$° coarser resolution but for a shorter period, from 1998 to 2012 [*Huffman et al*., 2007]. We further used monthly mean values of rainfall records for the in situ stations of Wewak, Madang, and Nadzab (see Figure 1a) obtained from the PCCSP.

For the Sepik River flow, we use three different products: the monthly mean values of freshwater discharge estimated at 1° resolution by *Dai and Trenberth* [2002] and *Fekete et al.* [2002], and the daily discharge recorded from 1970 to1997 at Ambuti, about 200 km in land from the river mouth [*Cappelaere and Virobo*, 1998]. Monthly climatology in P and river flow was computed over the maximum lengths of each interannual time series whenever available.

2-D SST, SSS, and wind data. We computed two SST monthly climatologies. The first climatology was obtained from the 1995–2010 high-resolution (4 km) nighttime daily maps of NOAA Advanced Very High

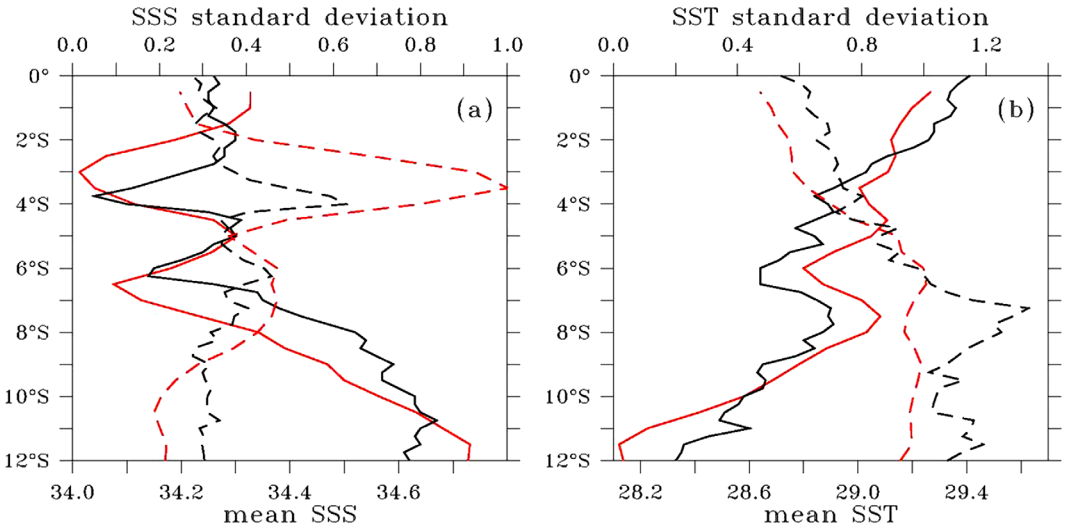

Figure 6. Long-term means (full lines, bottom scales) and standard deviations (dashed lines, upper scales) of (left) sea surface salinity and (right) sea surface temperature along the mean shipping track shown in Figure 1a. The black lines denote values obtained from VOS data, and the red lines from the CARS data.

Resolution Radiometer (AVHRR) Pathfinder Version 5.2 [*Kilpatrick et al*., 2001; *Vázquez-Cuervo et al*., 2010]. The second SST climatology and the corresponding SSS climatology were constructed from the 0.5° longitude by 0.5° latitude CARS product based on about 500 regional records [*Ridgway et al*., 2002]. The wind stress data are retrieved from the SeaWinds scatterometer onboard QuikSCAT. The climatology is derived from weekly maps delivered by the Center for Satellite Exploitation and Research (CERSAT), IFREMER, on a 0.5° × 0.5° grid between August 1999 and November 2009 [*Bentamy et al*., 2002].

Model data. We also used the global 1/12° Ocean General Circulation Model (OGCM) developed and operated by the DRAKKAR group [see *Barnier et al*., 2007], in its ORCA12.L46-MAL95 configuration [*Lecointre et al*., 2011]. The model, based on the OPA-NEMO *z* coordinate model [*Madec*, 2008], was forced by the ERA interim reanalysis over the 1978–2007 period. River flows were derived from the monthly climatology of *Dai and Trenberth* [2002]. The 3-D ocean state variables (temperature, salinity, and current) were saved every 5 days on the 1/12° grid mesh with a 6 m vertical resolution in the upper 250 m. Ignoring the first 11 years of spin-up, only values covering the 1989–2007 period were used to derive monthly mean climatology. Temperature, salinity, and current values in the model surface layer (0–6 m) were used to represent "surface" values; choosing values averaged with the mixed layer did not change our results. Note that terms of the mixed-layer temperature and salinity conservation equations were not saved online, preventing us to quantitatively assess their respective contribution to the SST and SSS changes. The model configuration and its evaluation are presented in more details in *Gourdeau et al*. [2014].

3. SSS and SST Mean and Standard Deviation

The mean and standard deviation values of the VOS-derived SSS and SST are shown in Figure 6, together with the corresponding CARS values. The mean VOS SSS values reach about 34.25 at the northern edge (0° latitude) and 34.6 at the southern edge (12°S) of the mean shipping track. Two remarkable SSS minima are present in the interior domain, one of less than 34.1 near 3.8°S at the latitude of the Sepik River mouth and the other one of less than 34.2 near 6.5°S at the latitude of the Markham River mouth and Vitiaz Strait. The meridional scales of the SSS relative minima, used as indicators of the rivers plumes, are of the order of 1.5° latitude, i.e., about 200 km given the SE-NW orientation of the mean shipping track. The two SSS minima correspond to the location of maximum SSS variability where the standard deviations reach values over 0.6 and 0.4, respectively. This correspondence suggests that an important part of the SSS variability is associated with the variability of the river flows, as discussed below.

The mean VOS SST values reach about 29.4°C at the northern edge of the mean shipping track, decreasing slightly to 28.3°C at its southern edge (Figure 6b). The along-track southward SST decrease is not linear,

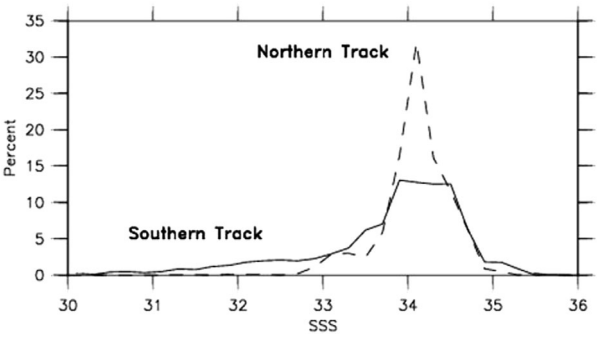

Figure 7. Probability density functions of SSS data per 0.2 bin in two successive 1° longitude by 0.5° latitude boxes located off the Sepik River mouth. The so-called southern box, contiguous to the coast, includes 5598 SSS values; the so-called northern box, contiguous to the southern box, includes 2505 values. All values were obtained during 1977–2009.

notably because there is a SST drop within about 6°S–7°S at the Vitiaz Strait latitude, also visible with the CARS data (Figure 2a) and to a lesser extent with the AVHRR data (not shown here). The SST drop could be related to intense vertical mixing due to the very energetic local horizontal circulation and vertical current shear (as suggested by *Cresswell* [2000]).

The mean VOS-derived SST and SSS values overall agree with the spatial distribution of CARS values presented in Figure 2. When sampling CARS data along the mean shipping track (Figure 6, red lines), the VOS-derived and CARS-derived SST and SSS means are generally similar, with however a tendency for the SSS minima in CARS to be located farther to the north off the Sepik River mouth and farther to the south off Vitiaz Strait. The standard deviation values derived from VOS and CARS also compare rather well in SSS and SST, except off the Sepik River mouth for SSS. This likely reflects that the VOS standard deviations values are based on monthly means covering the 1977–2009 period, whereas the CARS values are computed from all (nongridded) observations and hence include multiple time scales. When reconstructing SSS time series from semiannual and annual harmonics only (as provided in the database), the CARS standard deviation values reduce from 1.0 to 0.2 off the Sepik River mouth. It is also possible that the salinity variability in the 0–5 m surface layer, as obtained from CARS, is slightly greater than the one representative of the 0–10 m surface layer, as obtained from VOS. Besides, the DRAKKAR model mean values in SSS and SST sampled along the mean shipping track (not shown here) are similar to those shown in Figure 6, with however a 0.2°C warm bias in SST and 0.2 salty bias in SSS as compared to the VOS data. (These mean biases will be considered when presenting modeled values discussed below.)

A detailed examination of the VOS data spatial distribution (see Figure 4) indicates the presence of three distinct nearby shipping tracks off the Sepik River mouth at 3.8°S. Probability Density Functions (PDF) computed from all SSS observations collected in two 1° longitude by 0.5 latitude boxes centered on the two closest shipping tracks are shown in Figure 7. For the southern box, located about 25 km off the river mouth, the data distribution is by far non-Gaussian, with many values tailing off toward the negative end of the distribution. There, the difference between the median (33.98) and the mean (33.68) values, a common skewness indicator, is 0.3 that is 27% of the local standard deviation (1.13, i.e., about 10% greater than the CARS value in Figure 5a). For the northern box, located about 50 km of the river mouth, the negative skewness of the data distribution is much reduced, with a median (34.10) minus mean (34.08) difference of 0.02 that is only 5% of the standard deviation (0.4). The negative skewness in both PDF is clearly indicative of the Sepik river fresh water discharge. It also indicates that part of the differences we obtained between the VOS and CARS standard deviations in SSS (Figure 6a) could further result from the way we detected and discarded outliers using multiples of standard deviations then assuming Gaussian distribution, and/or that CARS data are located closer to the coast than the VOS data.

4. SSS and SST Seasonal Changes

The SST and SSS monthly climatology along the mean shipping track are shown from situ observations and model output in Figures 8a–8d, with values ranging from 27°C to 29.6°C for SST and 34 to 34.7 for SSS. (Note that the color bars of the observed and modeled figures are shifted by 0.2 to account for the model mean biases discussed above). Both SST and SSS go through large annual oscillations in the Solomon Sea (i.e., south of Vitiaz Strait, about 6.5°S), with the coldest and saltiest surface waters occurring in August. In

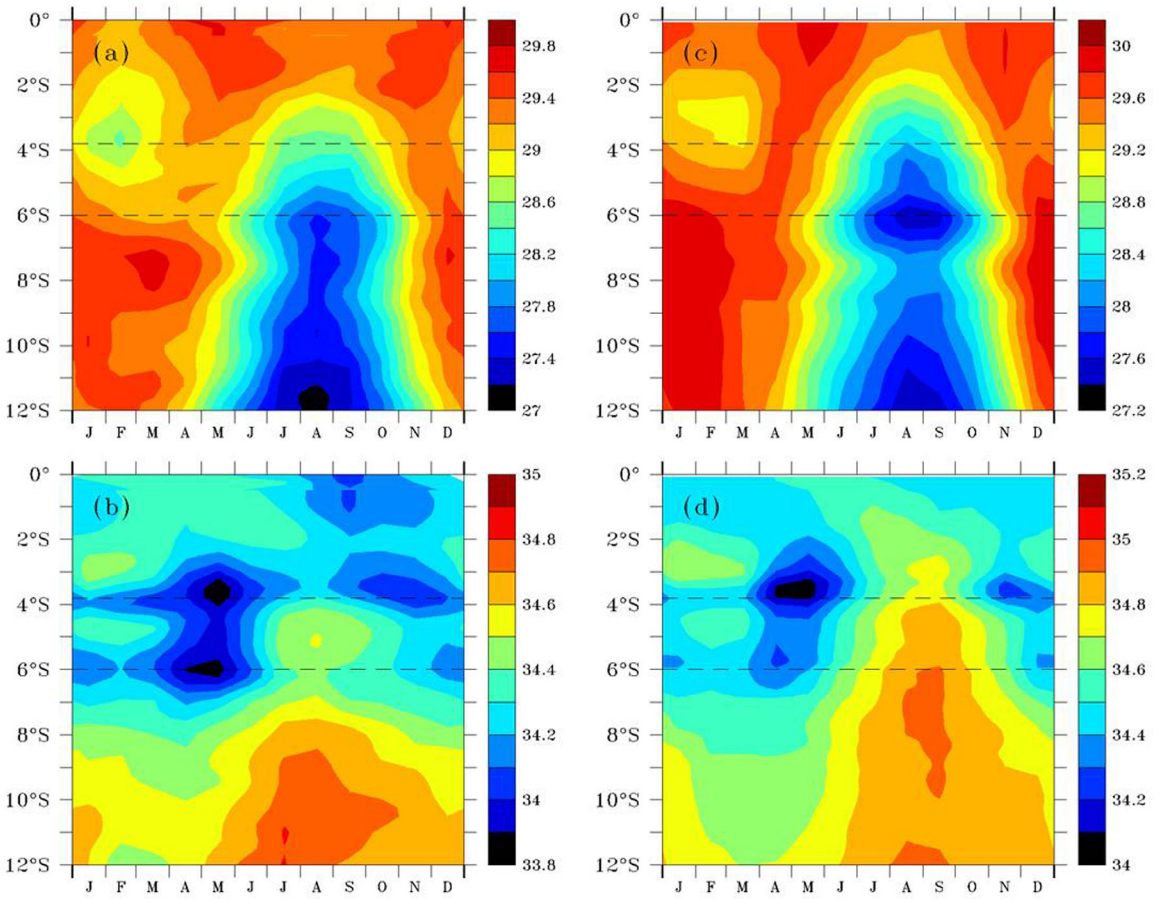

Figure 8. Monthly climatology of VOS-derived sea surface (a) temperature and (b) salinity, and (c and d) the corresponding model-derived values along the mean shipping track crossing the western Solomon and Bismarck Seas (see Figure 1a). Contour intervals are 0.1 for SSS, and 0.2°C for SST. Note the 0.2 units color bar shift between the observed and modeled figures. The thin horizontal dashed lines at 3.8°S and 6°S denote the latitudes of the Sepik and Markham River mouths, respectively.

contrast, both SST and SSS go through large semiannual oscillations in the Bismarck Sea, and slightly south of Vitiaz Strait for SSS, with the coldest SST and saltiest SSS in February and August.

4.1. Annual Oscillation in the Solomon Sea

Figure 8 clearly suggests that the quasi-simultaneous cooling and salinity increase in the Solomon Sea in austral winter results from the northwestward advection of relatively cold and salty waters coming from the southeastern part of the Solomon Sea to the Bismarck Sea. In situ observations of the surface circulation based on mooring and drifter data actually indicate that the NGCC has a well-marked annual cycle with maximum northwestward anomalies in austral winter [*Ueki et al*., 2003; *Hristova and Kessler*, 2012]. To strengthen these results, we further looked at the monthly climatology of the wind-induced (Ekman) and geostrophic components of the current. We found out that most of the Ekman current component variability occurs at the annual time scale (not shown), with maximum westward anomaly in August during the trade wind season (see Figure 3). A similar conclusion was obtained for the anomalous geostrophic current component we computed along seven satellite ground tracks, as exemplified for the months of February and August in Figure 9. It shows that the anomalous geostrophic component of the NGCC is directed to the northwest in August, to the southeast in February, and can be traced from the Solomon Sea entrance to the northern coast of PNG in the Bismarck Sea, consistent with the annual SST and SSS changes.

The VOS-derived and model-derived SST and SSS monthly climatology presented along the mean-shipping track in Figure 8 present a very good correspondence, giving us extra confidence in the already-evaluated model outputs [*Gourdeau et al*., 2014]. Two month averaged maps of modeled SST and SSS are then

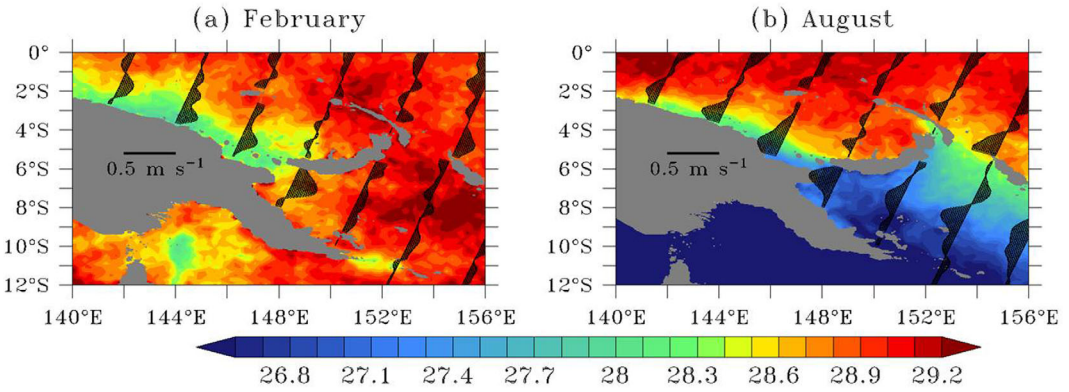

Figure 9. Mean sea surface temperature (color codes) in the PNG region from AVHRR and anomalous surface geostrophic current (arrows) along seven satellite ground tracks for the months of (a) February and (b) August. Units for SST are °C, and the current scale is reported in the PNG landmass.

shown in Figures 10 and 11, together with the corresponding absolute surface current field, to replace the along-track monthly climatology in a larger regional context. These maps confirm the May to October import of relatively cold and high-salinity waters coming from the southwest into the Solomon Sea, especially within a narrow vein flowing north of the southern tip of PNG. Undetectable from our along-track observations, the maps further suggest that relatively warm and salty waters coming from the equatorial band passing through Solomon Strait further modulate the Solomon Sea SST and SSS annual cycles, partly heating the cold SST and enhancing the high SSS coming from the southeast.

4.2. Semiannual Oscillation in the Bismarck Sea

Figure 8 shows that the coldest observed and simulated SST in the Bismarck Sea occur in August and February. The August minimum is consistent with horizontal advection in relation to the above-noted penetration of cold waters coming from the Solomon Sea through Vitiaz Strait. The role of horizontal advection is supported by the good agreement between the meridional scale of the northwestward geostrophic current anomalies and the cold SST patterns along the northern coast of PNG (Figure 9b), as well as with the consistent phasing of the modeled surface current and SST changes (Figure 10). The February minimum, in contrast, cannot be due to horizontal advection as there are inconsistent southeastward current anomalies at that time. Yet, the SST February minimum coincides with the occurrence of the seasonal coastal upwelling driven by northwesterly wind (see Figure 3a), as already documented in the literature [*Lukas*, 1986; *Hasegawa et al*., 2009, 2010; M.-H. Radenac et al., manuscript in preparation, 2014]. The spatial signature of this coastal upwelling clearly shows up using the AVHRR high-resolution SST product, with the appearance of coastal cooling along PNG in the Bismarck Sea (Figure 9a). The upwelling also slightly appears in the simulation, with a narrow band of relatively cold SST off the northern PNG coast in the Bismarck Sea (Figure 10a). Our analysis thus suggests that the cold phases of the SST semiannual oscillation along the mean shipping track in the Bismarck Sea owe their existence to two different processes: horizontal advection in austral winter and coastal upwelling in austral summer.

Regarding SSS in the Bismarck Sea (south of 2°S), Figure 8 indicates that the saltiest SSS occur in February and August. These semiannual SSS maxima thus coincide with the semiannual SST minima, suggesting that the SSS August maximum partly results from the import of high-salinity waters from the Solomon Sea via Vitiaz Strait, and the SSS February maximum from the import of high-salinity waters from below during the upwelling season. A back-of-the-envelope calculation however indicates that advection is likely insufficient to account for the amplitude of the semiannual SSS changes. For instance, the NGCC accelerated northwestward by 20 cm s^{-1} from May to August within 3°S–6°S. With a 0.05 SSS change between these two latitudes (Figure 6a), i.e., over a distance of about 550 km along the mean shipping track, the advective SSS term $U.S_x$ is about 0.15 in 3 months, which is insufficient to account for the observed 0.5–1 SSS decrease (Figure 8b). Hence, to examine other possible driving mechanisms, we first looked at changes in the Sepik River discharge given the outstanding correspondence between the location of the SSS minimum minimorum and the river mouth at 3.8°S. The monthly climatology of Sepik river discharge is shown in Figure 12a for three

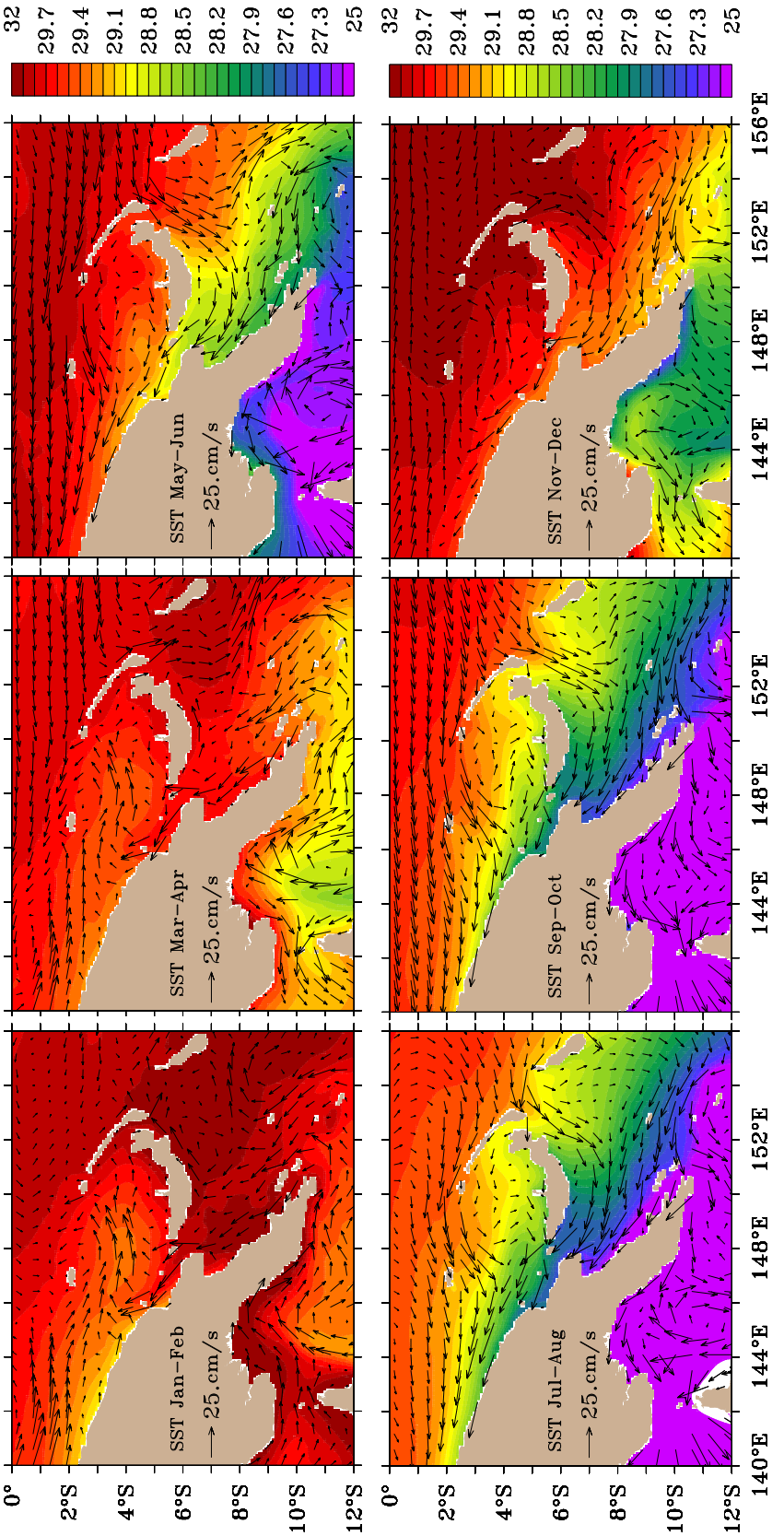

Figure 10. Bimonthly averaged values of the modeled SST (color codes; °C) and absolute surface currents (arrows) in the PNG region. Note the nonlinear color scale for values above 29.8°C and below 27.2°C.

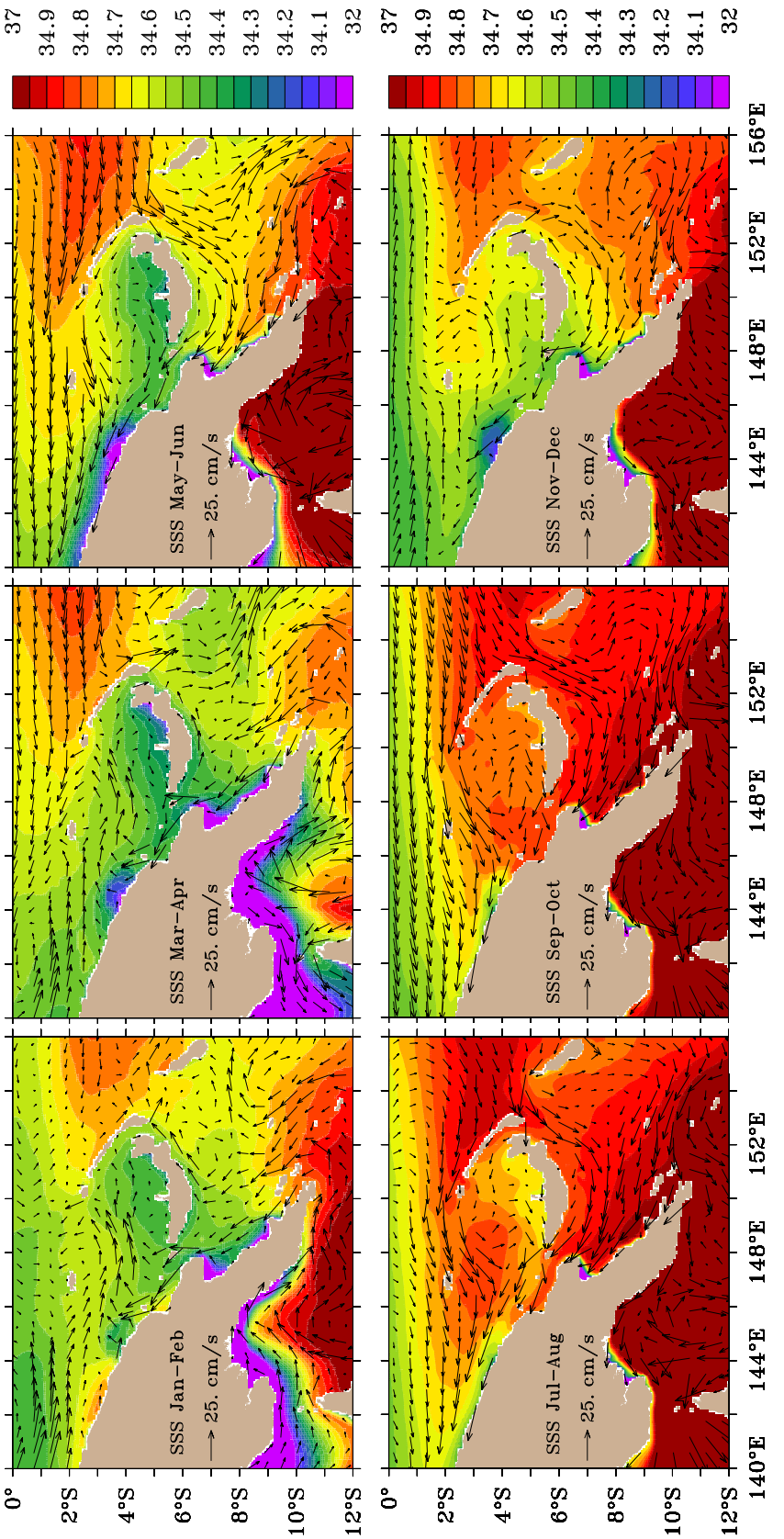

Figure 11. Bimonthly averaged values of the modeled SSS (color codes) and absolute surface currents (arrows) in the PNG region. Note the nonlinear color scale for values above 34.9 and below 34.1.

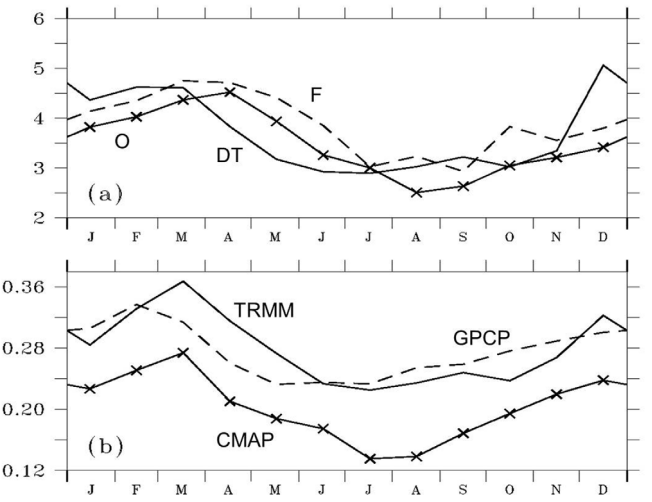

Figure 12. (a) Monthly climatology of the Sepik River discharge derived from (full line) *Dai and Trenberth* [2002], (dashed line) *Fekete et al.* [2002], and (full line with crosses) ORSTOM data. Note that the ORSTOM data were collected at Ambuti, i.e., about 200 km in-land. Units are 10^3 m^3/s. (b) Monthly climatology of precipitation averaged in the rectangle 140°E–145°E, 2.5°S–5°S bracketing the Sepik River catchment area, as derived from (full line) TRMM, (dashed line) GPCP, and (full line with crosses) CMAP products. Units are m/month. For comparison purpose, values of the vertical scale in Figure 12b were chosen so as to correspond to values of the vertical scale in Figure 12a given an estimated catchment area of 40,922 km^2 [*CAT*, 2002].

different products (see section 2). The annual mean is of the order of 3.5 × 10^3 m^3 s^{-1}, depending on the product. In perspective, this is about 1 order of magnitude smaller than the Yangtze River discharge in China, whose influence on SSS is large [*Delcroix and Murtugudde*, 2002]. The three products generally depict an annual oscillation, with maximum discharge in March/April and minimum discharge in August/September. (There are some differences amongst the products, whose range can be viewed as representative of the uncertainty). The SSS minimum in May at the latitude of the Sepik River mouth can thus be partly attributed to the river discharge annual maximum. It is likely that this also applies for the simultaneous SSS minimum occurring at 6°S at the latitude of the Markham River mouth (where we have no river flow data). The SSS signature of the Sepik River discharge is reproduced by the model, in March/April and November/December close to the river mouth, and in May/June as a plume of low salinity waters stretching northwestward along the northern PNG coast (Figure 11). The river plume is then much reduced during July/August, in agreement with the low phase of the annual river flow (Figure 12a) and with the apparent import of high-salinity waters coming from the northeast Bismarck Sea (Figure 11).

To further estimate the role of fresh water input on the SSS seasonal changes, we looked at P monthly climatology derived from in situ measurements collected at Wewak, Madang, and Nadzab (see locations in Figure 1a). Interestingly, values at Madang and Wewak tend to show a semiannual cycle with P maximum values in March-May and October-December (Figure 13). While phases of these semiannual cycles are to the first order consistent with the observed SSS semiannual cycle, they however show very different amplitudes, differing by as much as 100%. We also looked at the monthly climatology of precipitation for the CMAP, GPCP, and TRMM gridded products both along the mean-shipping track (not shown here) and averaged over the 140°E–145°E and 2.5°S–5°S rectangle roughly bracketing the Sepik River catchment area (Figure 12b). The amplitude of the CMAP, GPCP, and TRMM values also differ, by about 25% on a mean. Regarding the phase, the CMAP monthly climatological values show a well-marked annual cycle, with P maximum in March, logically leading the downstream outflow at the river mouth by 1–2 months, and P minimum in July/August. A seasonal P maximum is also visible with GPCP, in February, but the seasonal P minimum occurs earlier in May/June. We also note a tendency for TRMM to depict two annual maxima (in March and December).

In agreement with the processes accounting for the SST semiannual oscillation, our qualitative analysis thus suggests that the high-salinity phases of the SSS semiannual oscillation along the mean shipping track in the Bismarck Sea owe their

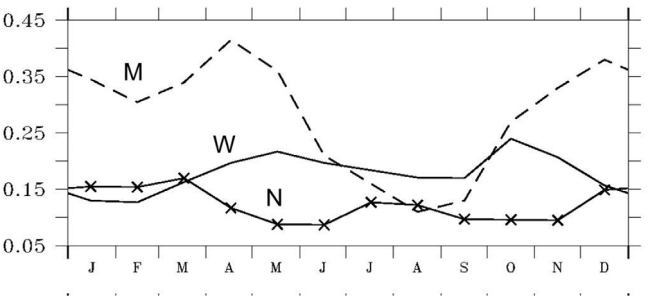

Figure 13. Monthly climatology of station-based precipitation at Wewak (W), Madang (M), and Nadzab (N; see Figure 1a for locations). Units are m/month.

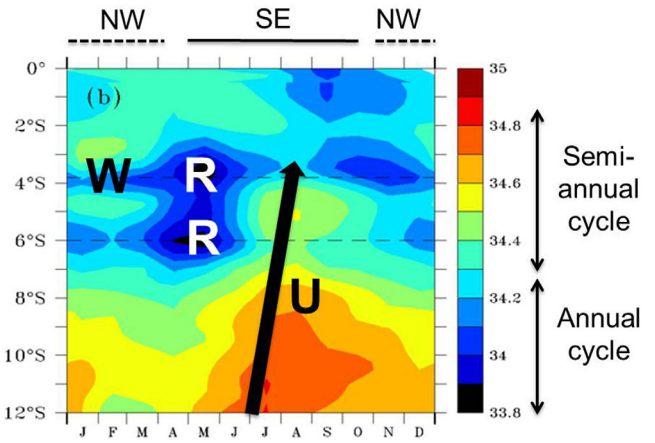

Figure 14. Monthly climatology of VOS-derived SSS in the western Solomon and Bismarck Seas (as in Figure 8b) and schematic of the three main driving mechanisms. U denotes horizontal advection, W vertical advection (coastal upwelling), and R freshwater input by the rainfall-induced Sepik and Markham river runoffs. Similar mechanisms apply for SST, except for river runoffs (R).

existence to two different processes: horizontal advection in austral winter and coastal upwelling in austral summer. Our data further suggest that the March/April maximum of the Sepik River discharge and probably (in absence of data) of the Markham River discharge reinforce the April/May minimum SSS appearing in between high-salinity phases. The rather poor amplitude and even phase agreements between the analyzed P data sets prevents us to be more conclusive regarding the role of rainfall in changing SSS at the semiannual cycle.

5. Conclusions and Discussions

The western equatorial Pacific Ocean, with SST warmer than 28°C, has long been recognized as an important region to explore in order to improve our understanding of climate variability, especially at the ENSO time scale [*WCRP*, 1990]. More recently, oceanic exchanges between the subtropics and the tropics, via interior transports and/or western boundary currents, have been hypothesized to play a role in ENSO low-frequency modulation and/or decadal changes. Monitoring and understanding such exchanges and the hydrological and circulation changes in the southwestern tropical Pacific have thus for a large part motivated the advent of the international SPICE program [*Ganachaud et al*., 2008]. As a contribution to this program, focusing on one of its topical geographical sectors, this study analyses the seasonal cycle of SST and SSS along a mean shipping track in the western Solomon and Bismarck Seas. It relies on in situ observations derived from VOS programs, on complementary in situ and satellite data to suggest driving mechanisms, and on a high-resolution model simulation to place the along-track SST and SSS changes in a larger spatial context.

We found that SST and SSS seasonal changes are dominated by the annual oscillation in the Solomon Sea, and the semiannual oscillation in the Bismarck Sea. In the Solomon Sea, the coldest and saltiest waters occur in July/August, mainly in response to the advection of cold and high-salinity waters coming from the southeast. In the Bismarck Sea, the coldest and saltiest waters still occur in July/August, also due to horizontal advection, and additionally happen in January/February when the northwest monsoon winds drive coastal upwelling. The low SSS values observed in April/May, stuck between the January/February and July/August semiannual SSS maxima, are found to be enhanced by the Sepik River discharge annual maximum. A schematic of the three main driving mechanisms is shown in Figure 14 for SSS.

Our analysis of driving mechanisms was done in a qualitative manner only, on one hand because we lack observations to properly evaluate all linear and a fortiori nonlinear terms involved in the SST and SSS conservation equations, and on the other hand because these terms were not saved online as the simulation procedure was originally defined for other purposes. Overlooking this limitation, the monthly mean climatology of SST and SSS along the mean shipping track was well reproduced with the 1/12° resolution model (and not with a $1/4^\circ$ resolution model, not discussed here), indicating the need for a model to resolve small-scale structures to be trustable in our studied region. We acknowledge that an interesting next step would be to compute online and save all terms of the mixed-layer temperature and salinity budget in the model, in order to quantify the respective contribution of different mechanisms driving SST and SSS seasonal variability.

Another aspect not addressed here is the ENSO influence on the regional SST and SSS distribution. Previous observational studies have shown there are usually colder-than-normal SST and drier-than-normal conditions during El Niño years, and vice versa during La Niña years [*Ropelewski and Halpert*, 1987; *Hristova and Kessler*, 2012]. To our knowledge, the regional ENSO-related SSS changes were not addressed in previous

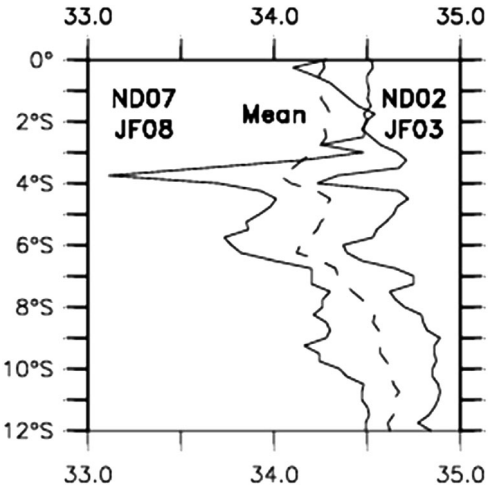

Figure 15. Sea surface salinity distribution along the mean shipping track shown in Figure 1a, averaged over the 4 month periods from (left-hand curve) November 2007 to February 2008 during a La Niña event, and from (right hand curve) November 2002 to February 2003 during an El Niño event. The dashed line reproduces the long-term mean VOS-derived SSS shown in Figure 5.

publications. *Singh et al.* [2011] however contrasted the basin-scale Eastern and Central Pacific (EP and CP) ENSO signature. For our studied region, their analysis shows positive SSS anomalies during EP El Niño events, whereas they show positive (negative) anomalies in the southern (northern) part of that region during CP El Niño events. Data and model simulations suggest large surface current variations in response to ENSO [*Ridgway et al.*, 1993; *Davis et al.*, 2012; *Hristova and Kessler*, 2012; *Melet et al.*, 2010b, 2013]. During an El Niño, northwestward current anomalies are observed through the southern Solomon Sea entrance and through Vitiaz and Solomon Straits; during a La Niña, the southward inflow entering at Solomon Strait is increased, and the northwestward flow through the southern entrance and through Vitiaz Strait may reverse. Our in situ SST and SSS data distribution shows too many data gaps (see Figure 5) to derive continuous time series in order to properly extract the signature of ENSO (unless using inappropriate extrapolations). Selecting two well-sampled periods as case studies, Figure 15 shows that SSS is saltier-than-average in November 2002 to February 2003, during an El Niño event, and fresher-than-average in November 2007 to February 2008, during a La Niña event. In perspective, we must however keep in mind that these two events are likely not representative of all events. The 2002–2003 CP El Niño event was actually placed third on record behind the very strong

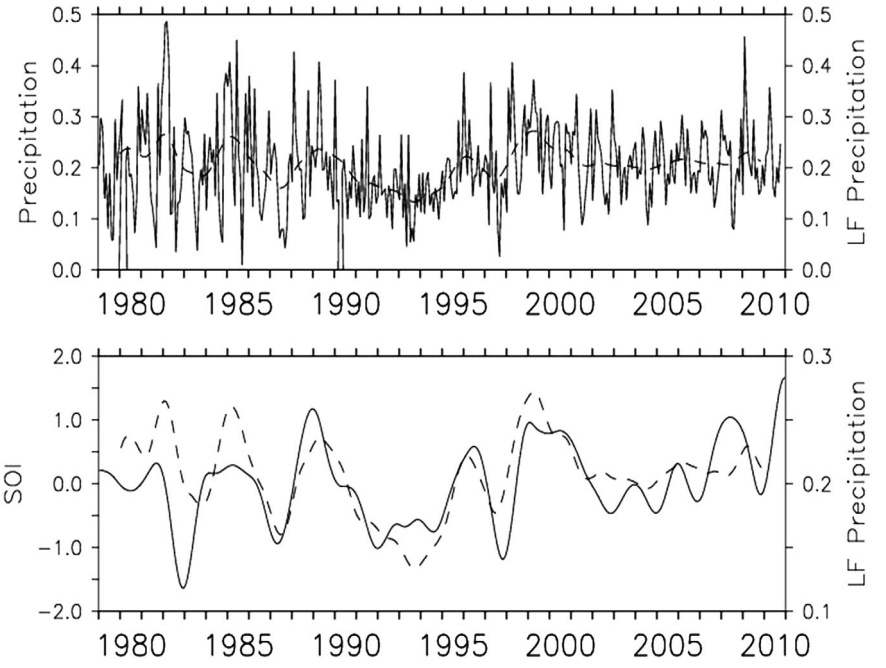

Figure 16. (top) Monthly values of 1979–2010 CMAP precipitation averaged in the rectangle 140°E–145°E, 2.5°S–5°S roughly bracketing the Sepik River catchment area. The full line represents the original time series and the dashed line the 25 month Hanning filtered time series. (bottom) Comparison between the 25 month Hanning filtered time series of (dashed line) precipitation and (full line) SOI. Units for precipitation are m/month.

1982–1983 and 1997–1998 EP El Niño events when characterized by the easternmost displacement of the equatorial eastern edge of the warm pool (used as an indicator of ENSO strength) [see *Delcroix and Picaut*, 1998], and the 2007–2008 La Niña was placed first on record when characterized by the westernmost displacement since 1976 [*Singh et al*., 2011, Figure 10]. Focusing off the Sepik river mouth where the ENSO-related SSS signal looks maximum, the contrasted El Niño/La Niña signature is coherent with the rainfall expected changes and related Sepik river outflow modifications. As shown in Figure 16, there is actually a very good correlation between the interannual P changes in the Sepik River catchment area (used as a river outflow index, see Figure 12) and the Southern Oscillation Index (SOI), with a decrease of P during El Niño years and an increase during La Niña years. Hence, these overall features suggests that the strong contrasted SSS signature of El Niño and La Niña events south and near the Sepik River mouth could, at least partly, results from changes in horizontal advection and rainfall-related Sepik River discharge. A recent and detailed study of rainfall changes from in situ data collected in the PNG region however indicates that the relationship between ENSO and P changes is very complex and can vary from one ENSO event to another as well as from one subregion to another [see *Smith et al*., 2013, Figure 6]. A dedicated simulation, validated with our in situ observations, would thus clearly help to further explore all causes for SST and SSS changes in the Solomon and Bismarck Seas.

Acknowledgments

The SST and SSS data derived from TSG instruments installed onboard voluntary observing ships were collected, validated, archived, and made freely available by the French Sea Surface Salinity Observation Service (http://www.legos.obs-mip.fr/observations/sss/). We benefited from other freely available data sets, including along-track altimeter-derived sea level anomaly from the CTOH (http://ctoh.legos.obs-mip.fr/), precipitation data from CMAP (http://www.esrl.noaa.gov/psd/data/gridded/data.cmap.html), GPCP (http://www.esrl.noaa.gov/psd/data/gridded/data.gpcp.html), and TRMM (http://disc.sci.gsfc.nasa.gov/precipitation/documentation/TRMM_README/TRMM_3B42_readme.shtml), and station-based precipitation from the PCCSP (http://www.pacificclimatechangescience.org/). Comments from two anonymous reviewers were appreciated. This work is a contribution to the Solwara proposal supported by the French ANR.

References

Adler, R. F., G. J. Huffman, D. T. Bolvin, S. Curtis, and E. J. Nelkin (2000), Tropical rainfall distributions determined using TRMM combined with other satellite and rain gauge information, *J. Appl. Meteorol.*, *39*(12), 2007–2023, doi:10.1175/1520-0450(2001)040<2007:TRDDUT>2.0.CO.2.

Barnier, B., et al. (2007), Eddy-Permitting ocean circulation hindcasts of past decades, *CLIVAR Exchanges*, *12*, 8–10.

Bentamy, A., Y. Quilfen, and P. Flament (2002), Scatterometer wind fields: A new release over the decade 1991–2001, *Can. J. Remote Sens.*, *28*(3), 431–449.

Birol, F., M. Cancet, and C. Estournel (2010), Aspects of the seasonal variability of the Northern Current (NW Mediterranean Sea) observed by altimetry, *J. Mar. Syst.*, *81*(4), 297–311, doi:10.1016/j.jmarsys.2010.01.005.

Burns, K. A., G. Brunskill, D. Brinkman, and I. Zagorskis (2008), Organic carbon and nutrient fluxes to the coastal zone from the Sepik River outflow, *Cont. Shelf Res.*, *28*, 283–301.

Butt, R., and E. Lindstrom (1994), Currents off the east coast of New Ireland, Papua New Guinea, and their relevance to regional undercurrents in the western equatorial Pacific Ocean, *J. Geophys. Res.*, *99*(C6), 12,503–12,514.

Cappelaere, B., and M. Virobo (1998), *SEPIK River Flood Forecasting: Summary of Study Performed at ORSTOM's Hydrology Lab, Montpellier, France, and Bureau of Water Resources, Port Moresby, Papua New Guinea* (internal documentation).

CAT (2002), *Catalogue of Rivers for the Southeast Asia and the Pacific*, vol. IV, edited by R. Ibbitt et al., UNESCO IHP-Publ, UNESCO Regional Steering Committee for the Southeast Asia and the Pacific.

Cravatte, S., A. Ganachaud, Q.-P. Duong, W. S. Kessler, G. Eldin, and P. Dutrieux (2011), Observed circulation in the Solomon Sea from SADCP data, *Prog. Oceanogr.*, *88*, 116–130.

Cresswell, G. (2000), Coastal currents of northern Papua New Guinea, and the Sepik River outflow, *Mar. Freshwater Res.*, *51*, 553–564.

Dai, A., and K. Trenberth (2002), Estimates of freshwater discharge from continents: Latitudinal and seasonal variations, *J. Hydrometerol.*, *3*, 660–667.

Davis, R. E., W. S. Kessler, and J. T. Sherman (2012), Gliders measure western boundary current transport from the South Pacific to the equator, *J. Phys. Oceanogr.*, *42*(11), 2001–2013.

Delcroix, T., and C. Hénin (1991), Seasonal and interannual variations of sea surface salinity in the tropical Pacific Ocean, *J. Geophys. Res.*, *96*(C12), 22,135–22,150.

Delcroix, T., and M. McPhaden (2002), Interannual sea surface salinity and temperature changes in the western Pacific warm pool during 1992–2000, *J. Geophys. Res.*, *107*(C12), 8002, doi:10.1029/2001JC000862.

Delcroix, T., and R. Murtugudde (2002), Sea surface salinity changes in the East China Sea during 1997–2001: Influence of the Yangtze river, *J. Geophys. Res.*, *107*(C12), 8008, doi:10.1029/2001JC000893.

Delcroix, T., and J. Picaut (1998), Zonal displacements of the western equatorial Pacific fresh pool, *J. Geophys. Res.*, *103*(C1), 1087–1098.

Delcroix, T., M. McPhaden, A. Dessier, and Y. Gouriou (2005), Time and space scales for sea surface salinity in the tropical oceans, *Deep Sea Res., Part I*, *52*(5), 787–813, doi:10.1016/j.dsr.2004.11.012.

Donguy, J. R., and C. Hénin (1976), Anomalous navifacial salinities in the tropical Pacific Ocean, *J. Mar. Res.*, *34*, 355–364.

Fekete, B. M., C. J. Vörösmarty, and W. Grabs (2002), High-resolution fields of global runoff combining observed river discharge and simulated water balances, *Global Biogeochem. Cycles*, *16*(3), 1042, doi:10.1029/1999GB001254.

Ganachaud, A., et al. (2008), *Southwest Pacific Ocean Circulation and Climate Experiment (SPICE). Part II. Implementation Plan*, NOAA OAR special report, CLIVAR Publ. Ser., vol. 133, 36 pp., Int. CLIVAR Proj. Off. NOAA/OAR/PMEL, Seattle, Wash.

Gourdeau, L., J. Verron, A. Melet, W. Kessler, F. Marin, and N. Djath (2014), Exploring the mesoscale activity in the Solomon Sea: A complementary approach with a numerical model and altimetric data, *J. Geophys. Res.*, in press.

Grenier, M., S. Cravatte, B. Blanke, C. Menkes, A. Koch-Larrouy, F. Durand, A. Melet, and C. Jeandel (2011), From the western boundary currents to the Pacific Equatorial Undercurrent: Modeled pathways and water mass evolutions, *J. Geophys. Res.*, *116*, C12044, doi:10.1029/2011JC007477.

Hasegawa, T., K. Ando, K. Mizuno, and R. Lukas (2009), Coastal upwelling along the north coast of Papua New Guinea and SST cooling over the Pacific warm pool: A case study for the 2002/03 El Niño event, *J. Oceanogr.*, *65*, 817–833.

Hasegawa, T., K. Ando, K. Mizuno, R. Lukas, B. Taguchi, and H. Sasaki (2010), Coastal upwelling along the north coast of Papua New Guinea and El Niño events during 1981–2005, *Ocean Dyn.*, *60*, 1255–1269.

Hénin, C., and J. Grelet (1996), A merchant ship thermo-salinograph network in the Pacific Ocean, *Deep Sea Res., Part I*, *43*(11), 1833–1855.

Higgins, H. W., D. J. Mackey, and L. Clementson (2006), Phytoplankton distribution in the Bismarck Sea north of Papua New Guinea: The effects of the Sepik river outflow, *Deep Sea Res., Part I*, *53*, 1845–1863.

Hisard, P., Y. Magnier, and B. Wauthy (1969), Comparison of the hydrographic structure of equatorial waters north of New Guinea and at 170°E, *J. Mar. Res.*, *27-2*, 191–205.
Hristova, H., and W. Kessler (2012), Surface circulation in the Solomon Sea derived from Lagrangian drifter observations, *J. Phys. Oceanogr.*, *42*, 448–458, doi:10.1075/JPO-D-11–099.1.
Huffman, G., R. F. Adler, D. T. Bolvin, G. Gu, E. J. Nelkin, K. P. Bowman, Y. Hong, E. F. Stocker, and D. B. Wolff (2007), The TRMM multisatellite precipitation analysis (TMPA): Quasi-global, multiyear, combined-sensor precipitation estimates at fine scales, *J. Hydrometeorol.*, *8*(1), 38–55, doi:10.1175/JHM560.1.
Kilpatrick, K. A., G. P. Podestá, and R. Evans (2001), Overview of the NOAA/NASA advanced very high resolution radiometer Pathfinder algorithm for sea surface temperature and associated matchup database, *J. Geophys. Res.*, *106*(C5), 9179–9197, doi:10.1029/1999JC000065.
Kineke, G. C., K. J. Woolfe, S. A., Kuehl, J. D. Milliman, T. M. Dellapena, and R. G. Purdon (2000), Sediment export from the Sepik River, Papua New Guinea: Evidence for a divergent sediment plume, *Cont. Shelf Res.*, *20*, 2239–2266.
Lagerloef, G. S. E., G. T. Mitchum, R. B. Lukas, and P. P. Niiler (1999), Tropical Pacific near-surface currents estimated from altimeter, wind, and drifter data, *J. Geophys. Res.*, *104*(C10), 23,313–23,326.
Lecointre, A., J. M. Molines, and B. Barnier (2011), Definition of the interannual experiment ORCA12.L46-MAL95, 1989–2007, Internal *Rep. LEGI-DRA 21-10-2011*, 25 pp., MEOM-LEGI—CNRS, Grenoble, France.
Lindstrom, E., R. Lukas, R. Fine, E. Firing, S. Godfrey, G. Meyers, and M. Tsuchiya (1987), The western equatorial Pacific Ocean circulation study, *Nature*, *330*, 533–537.
Lukas, R. (1986), Upwelling along the Papua New Guinea coast, paper presented at the Symposium on Marine Science of the Western Pacific: The Indo Pacific Convergence, Townsville, Australia, 1–6 Dec. Intergovernmental Oceanographic Commission (IOC), Program Group for the Western Pacific (WESTPAC).
Mackey, D., J. O'Sullivan, and R. Watson (2002), Iron in the western Pacific: A riverine or hydrothermal source for iron in the Equatorial Undercurrent?, *Deep Sea Res., Part I*, *49*, 877–893.
Madec (2008), NEMO ocean engine, in *Note du Pôle Modélisation*, vol. 27, 300 pp., Inst. Pierre-Simon Laplace, France.
Melet, A., L. Gourdeau, W. Kessler, J. Verron, and J. M. Molines (2010a), Thermocline circulation in the Solomon Sea: A modeling study, *J. Phys. Oceanogr.*, *40*(6), 1302–1319.
Melet, A., L. Gourdeau, and J. Verron (2010b), Variability in Solomon Sea circulation derived from altimeter sea level data, *Ocean Dyn.*, *60*(4), 883–900.
Melet, A., L. Gourdeau, J. Verron, and N. Djath (2013), Solomon Sea circulation and water mass modifications: Response at ENSO time-scales, *Ocean Dyn.*, *63*, 1–19, doi 10.1007/s10236-012-0582-0.
Milliman, J. D., and K. Farnsworth (2011), *River Discharge to the Coastal Ocean: A Global Synthesis*, 392 pp., Cambridge Univ. Press, Cambridge, U. K.
Palmer, T. N., and D. A. Mansfield (1984), Response of two atmospheric general circulation models to sea-surface temperature anomalies in the tropical east and west Pacific, *Nature*, *310*(5977), 483–485, doi:10.1038/310483a0.
Picaut, J., and R. Tournier (1991), Monitoring the 1979–1985 equatorial Pacific current transports with expendable bathythermograph data, *J. Geophys. Res.*, *96*(S01), 3263–3277.
Prunier-Mignot, M., D. Varillon, L. Foucher, J. M. Ihily, B. Buisson, F. Masia, C. Hénin, M. Ioualalen, and T. Delcroix (1999), *Users Guide for Thermosalinograph Installation and Maintenance Aboard a Ship*, Océanogr. Phys., vol. 13, 102 pp., Cent. ORSTOM de Nouméa, New Caledonia.
Qin, H., H. Kawamura, and Y. Kawaii (2007), Detection of hot event in the equatorial Indo-Pacific warm pool using advanced satellite SST, solar radiation, and wind speed, *J. Geophys. Res.*, *112*, C07015, doi:10.1029/2006JC003969.
Ramesh, N., and R. Murtugudde (2012), All flavours of ENSO have similar early subsurface origins, *Nat. Clim. Change*, *3*, 42–46, doi:10.1038/NCLIMATE1600.
Ridgway, K. R., J. S. Godfrey, G. Meyers, and R. Bailey (1993), Sea level response to the 1986–1987 El Niño-Southern event in the western Pacific in the vicinity of Papua New Guinea, *J. Geophys. Res.*, *98*(9), 16,387–16,395.
Ridgway, K. R., J. R. Dunn, and J. L. Wilkin (2002), Ocean interpolation by four-dimensional weighted least squares—Application to the waters around Australasia, *J. Atmos. Oceanic Technol.*, *19*(9), 1357–1375.
Roblou, L., J. Lamouroux, J. Bouffard, F. Lyard, M. Le Henaff, A. Lombard, P. Marsaleix, P. De Mey, and F. Birol (2011), Post-processing altimeter data toward coastal applications and integration into coastal models, in *Coastal Altimetry*, chap. 8, edited by S. Vignudelli et al., pp. 217–246, Springer, Berlin.
Ropelewski, C. F., and M. S. Halpert (1987), Global and regional scale precipitation patterns associated with the El Niño/Southern oscillation, *Mon. Weather Rev.*, *115*, 1606–1626.
Ryan, J. P., I. Ueki, Y. Chao, H. Zhang, P. S. Polito, and F. P. Chavez (2006), Western Pacific modulation of large phytoplankton blooms in the central and eastern equatorial Pacific, *J. Geophys. Res.*, *111*(G2), G02013, doi:10.1029/2005JG000084.
Singh, A., T. Delcroix, and S. Cravatte (2011), Contrasting the flavors of El Niño Southern Oscillation using sea surface salinity observations, *J. Geophys. Res.*, *116*, C06016, doi:10.1029/2010JC006862.
Slemons, L. O., B. Paul, J. Resing, and J. W. Murray (2013), Particulate iron, aluminum, and manganese in the Pacific equatorial undercurrent and low latitude western boundary current sources, *Mar. Chem.*, *142*, 54–67, doi:10.1016/j.marchem.2012.08.003.
Smith, I., A. Moise, K. Inape, B. Murphy, R. Colman, S. Power, and C. Chung (2013), ENSO-related rainfall changes over the New Guinea region, *J. Geophys. Res.*, *188*, 1–11, doi:10.1002/jgrd.50818.
Ueki, I., Y. Kashino, and Y. Kuroda (2003), Observation of current variations off the New Guinea coast including the 1997–1998 El Niño period and their relationship with Sverdrup transport, *J. Geophys. Res.*, *108*(C7), 3243, doi:10.1029/2002JC001611.
Vázquez-Cuervo, J., E. M. Armstrong, K. S. Casey, R. Evans, and K. Kilpatrick (2010), Comparison between the Pathfinder versions 5.0 and 4.1 sea surface temperature datasets: A case study for high resolution, *J. Clim.*, *23*, 1047–1059.
Waliser, D. E., and N. Graham (1993), Convective cloud systems and warm pool sea surface temperatures: Coupled interactions and self-regulation, *J. Geophys. Res.*, *98*(D7), 12,881–12,893.
World Climate Research Program (1990), Scientific Plan for the TOGA Coupled Ocean Atmosphere Response Coupled Experiment, Publ. Ser. 3. International TOGA projet office. WMO, Geneva, Switzerland.
Wyrtki, K. (1961), Physical oceanography of the southeast Asian waters, in Scientific Results of Marine Investigations of the South China Sea and the Gulf of Thailand, 1959–1961, vol. 2, NAGA report, The Univ. of Calif., Scripps Inst. of Oceanogr., La Jolla, California.
Xie, P., and P. Arkin (1998), Global monthly precipitation estimates from satellite-observed outgoing longwave radiation, *J. Clim.*, *11*(2), 137–164.